

Audelia G. Dharmawan

Engineering Product Development,
Singapore University of Technology and Design,
Singapore 487372
e-mail: audelia@sutd.edu.sg

Priti Xavier

Engineering Product Development,
Singapore University of Technology and Design,
Singapore 487372
e-mail: priti.xavier@gmail.com

Hassan H. Hariri

Mechanical and Mechatronic Engineering,
Rafik Hariri University,
Mechref, Lebanon
e-mail: haririhh@rhu.edu.lb

Gim Song Soh¹

Engineering Product Development,
Singapore University of Technology and Design,
Singapore 487372
e-mail: sohgimsong@sutd.edu.sg

Avinash Baji

Department of Engineering,
La Trobe University,
Bundoora, VIC 3086, Australia
e-mail: a.baji@latrobe.edu.au

Roland Bouffanais

Engineering Product Development,
Singapore University of Technology and Design,
Singapore 487372
e-mail: bouffanais@sutd.edu.sg

Shaohui Foong

Engineering Product Development,
Singapore University of Technology and Design,
Singapore 487372
e-mail: foongshaohui@sutd.edu.sg

Hong Yee Low

Engineering Product Development,
Singapore University of Technology and Design,
Singapore 487372
e-mail: hongyee_low@sutd.edu.sg

Kristin L. Wood

Engineering Product Development,
Singapore University of Technology and Design,
Singapore 487372
e-mail: kristinwood@sutd.edu.sg

Design, Modeling, and Experimentation of a Bio-Inspired Miniature Climbing Robot With Bilayer Dry Adhesives

This paper presents the design, modeling, and analysis of the force behavior acting on a wheel-legs (whegs) type robot which utilizes bilayer dry adhesives for wall-climbing. The motion of the robot is modeled as a slider-crank mechanism to obtain the dynamic parameters of the robot during movement. The required forces and moment to maintain equilibrium as the robot is in motion is then extensively analyzed and discussed. Following the analysis, fundamental measures to attain an operative climbing robot, such as adhesive requirement and torque specification, are then identified. The outcomes of the analysis are verified through experiments and working prototypes that are in good agreement with the design guidelines. [DOI: 10.1115/1.4042457]

1 Introduction

The use of robots for autonomous intelligent surveillance and reconnaissance is gaining prominence. Typical tasks include mapping, monitoring, detection, tracking, and search and rescue

operations, with each requiring robots of a certain set of capabilities. Typically, these are achieved through the use of unmanned aerial vehicles (UAVs) or unmanned ground vehicles (UGVs), depending on the type of terrains and mission requirements. However, these robots are typically bulky to be used as soldier systems, which make the use of a collaborative swarm of miniature robots to achieve these tasks attractive [1].

Compared to UAVs, UGVs have the advantage of accurately locating ground targets [2]. Various developments of miniature UGVs for autonomous intelligent surveillance and

¹Corresponding author.

Contributed by the Mechanisms and Robotics Committee of ASME for publication in the JOURNAL OF MECHANISMS AND ROBOTICS. Manuscript received October 6, 2018; final manuscript received December 21, 2018; published online February 22, 2019. Assoc. Editor: Andreas Mueller.

reconnaissance, each with its unique capabilities, can be found in the literature, for example spherical robot Virgo [3], piezoelectric robot Pisces [4], jumping robot Scout [5], tracked robot MTRR [6], and climbing robot City-climber [7]. Among these, robots that are capable of scaling vertical surfaces exhibit many benefits, such as a highly expanded workspace and the ability to reach or accomplish otherwise impossible spots or tasks. In addition, being small offers capability to navigate into tight narrow spaces, something which even UAVs find difficult due to the precision involved.

Several means can be utilized to realize climbing robots, such as through magnetic attachment [8], vacuum suction [7], gripping capability [9], and electro-adhesive technology [10]. Each approach has its own strengths and weaknesses. Magnets are strong but only work on ferrous surfaces. Suction requires bulky compressed air and completely smooth surfaces in order to establish an ideal seal. On the other hand, gripping does not work on smooth surfaces and requires looking for randomly located hand-holds. Electro-adhesion requires high voltage in the order of kV. Recently, climbing robots utilizing dry adhesives have been proposed to overcome those drawbacks [11–15]. For a comprehensive review, refer to Ref. [16]. Dry adhesion is inspired by gecko's unique ability and agility in climbing diverse surfaces. Using dry adhesion, robots are able to climb irrespective of the surface material and properties or air pressure availability. Dry adhesives are also lightweight, power efficient, and operationally quiet. In this paper, we utilize bilayer dry adhesives for our climbing robot.

In terms of locomotion mechanism, our climbing robot has a similar structure as Mini-Whegs [17] and Waalbot [18]. It has been observed from Nature that the mechanism for attachment to surfaces in climbing animals is completely different from the one associated with detachment [19]. The general principle is found to be entire-surface attachment and peeling-like detachment such that strong adhesion can be instantaneously generated while minimal effort is required during contact release. For miniature robot systems, designing bulky mechanisms to fulfill this locomotion principle is undesirable. A more effective approach is to employ wheel-leg configuration with compliant adhesives to produce the required motion [20].

Despite Mini-Whegs' outstanding performance in climbing surfaces, little in-depth study can be found in the literature which theoretically models and analyzes the design requirements and capabilities of this type of robot. This paper adapts the approach introduced in Ref. [21] to: (i) analyze our miniature climbing robot (Orion), (ii) generate its design criteria, and (iii) predict its performance. Building up from the literature, this paper expands the approach to incorporate the modeling of the movement of the robot for a more comprehensive force analysis during the motion of the robot. This paper also provides further insight into several aspects that were previously absent such as the significance of the

tail effect on the overall robot's equilibrium, motor torque requirement, as well as design criteria verification.

2 The Climbing Robot: Orion

Shown in Fig. 1, the architecture of our power-autonomous miniature climbing robot, Orion, consists of a robot chassis (tail) carrying the electronics and two DC motors each driving a wheel-leg (wheg) with four "flaps" equipped with bilayer dry adhesives. There is a 4:1 gear reduction between the motor and the whegs. The mass of the physical robot prototype is 71.5 g.

2.1 The Bilayer Dry Adhesive.

The bilayer synthetic gecko-inspired adhesive used here comprises of a layer of micropillar adhesive surface (polydimethylsiloxane (PDMS)) and an unstructured backing layer of polymer (3 M very high bond (VHB) tape) of different elastic behavior. A gradient in the viscoelastic property is thus created in the bilayer adhesive with one layer being more elastic and the other being more dissipative [22]. A series of studies has shown that a bilayer adhesive with backing layer of linearly stiff carbon fiber in soft elastomeric adhesives imparts equal load sharing and also reduces the deformation of the soft elastomer layer [23–26]. In our case, we use a viscoelastic tape as backing layer of a lower modulus than the elastomeric adhesive due to the high energy absorption characteristic of the tape. The viscoelastic foam core of the 3 M VHB tape absorbs the tensile stress, spreads the stress throughout the entire bond, and possesses high internal cohesive strength [27]. It was also observed from various reports in the literature that the addition of a foam backing layer enhances the adhesive force of PDMS [28,29].

The elastomeric dry adhesive footpad was fabricated from elastomer PDMS, Sylgard184 (Dow Corning, Midland, MI). PDMS is a silicone-based elastomeric polymer which is thermally cured through a crosslinking reaction. The micropillars footpads were fabricated by soft lithography technique which can duplicate structures by replica molding from a SU-8 master mold (hole mold). The PDMS monomer and the cross linker in the ratio of 10.5:1 were mixed and degassed in a centrifugal mixer (Thinky Mixer), poured into micropatterned SU-8 mold to the desired thickness, and cured at 80 °C for 1.5 h in a carefully leveled oven. The PDMS is demolded from the master mold after curing. The resulting structures were pillars with 2 μm diameter, 2 μm height, and 6 μm center-to-center spacing in a hexagonal distribution (Fig. 2). The patterns were distributed as a square of area 1 cm², and each square patch has a distance of approximately 1 cm² between each other. Hence, an adhesive flap of 10 cm² has 5 cm² area with these patterns and the rest of the area is unpatterned. This adhesive was then attached to the 3 M Scotch VHB tape 4607, forming a PDMS/tape composite bilayer adhesive, which is being used in the climbing robot.

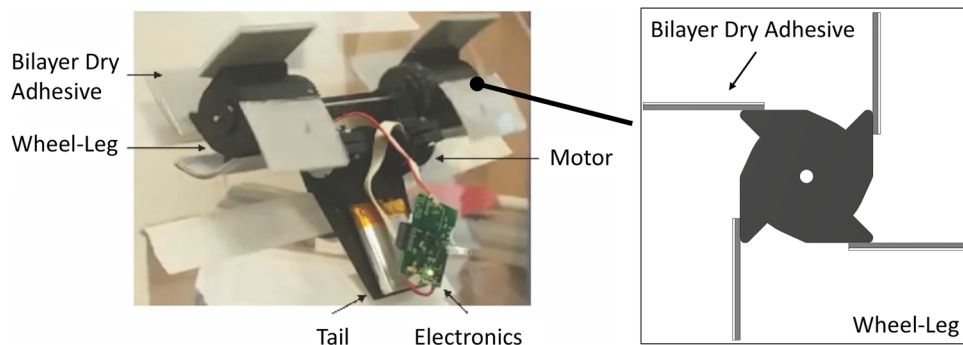


Fig. 1 Photograph of prototype Orion with wheel-leg configuration of four flaps climbing an inclined acrylic surface

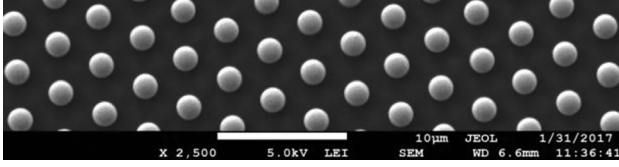


Fig. 2 Scanning electron micrograph of PDMS micropillars used in our dry adhesive

2.2 Adhesive Characterization. Adhesive material is characterized by how much adhesive force is generated given a preload force. Typically, adhesion is greater than preload for low preload pressures and saturates to a maximum adhesion value at high preload pressures. The bilayer adhesive used here was characterized for its adhesion through measurement on a custom-made setup [30] consisting of a computer numerical control (CNC) milling machine, a digital balance with a range of ± 300 g and a precision of 0.01 g, and an acrylic piece of 25 mm \times 25 mm attached to the drill chuck of the CNC milling machine to simulate the climbing wall. A 20 mm \times 20 mm adhesive specimen was loaded onto the center of the weighing pan of the balance and a normal preload ranging from 2 g to 250 g was applied by rotating the vertical feed handwheel of the CNC machine to lower the acrylic piece onto the adhesive. Once the positive balance reading reached the desired preload value, the acrylic piece was withdrawn and the negative balance reading during the withdrawal represented the normal adhesive force of the specimen. Data recorded then represent the normal adhesive force corresponding to the applied preload force which characterizes the bilayer adhesive used here.

3 Robot Modeling and Force Analysis

In this section, we describe our robot locomotion model and the force analysis we performed in order to obtain the climbing robot requirements.

3.1 Robot Motion Model. To study the robot behavior during each flap contact cycle, we model the robot movement as a slider-crank mechanism to capture the dynamically changing geometric parameters for use in the force analysis. As portrayed in Fig. 3, during each flap contact cycle, the robot's movement resembles a slider-crank mechanism that rotates from $\psi = 0$ deg to $\psi = 90$ deg, after which the rotational pivot switches to the next successive flap and the motion repeats. Using the analysis of the RRRP (revolute revolute revolute prismatic) linkage [31], the positions of the pivot points **A** and **B**, and the point **C** in the coupler (representing the position of the robot's center of gravity (CG)) relative to the frame at pivot point **O**, as shown in Fig. 4, can be expressed in terms of the input angle ζ as

$$\mathbf{A} = \begin{Bmatrix} r \cos \zeta \\ r \sin \zeta \end{Bmatrix} \quad (1)$$

$$\mathbf{B} = \begin{Bmatrix} s \\ e \end{Bmatrix} \quad (2)$$

$$\mathbf{C} = \begin{Bmatrix} r \cos \zeta + d \cos(\zeta + \phi - \alpha) \\ r \sin \zeta + d \sin(\zeta + \phi - \alpha) \end{Bmatrix} \quad (3)$$

where

$$s = r \cos \zeta - \sqrt{L^2 - e^2 + 2er \sin \zeta - (r \sin \zeta)^2} \quad (4)$$

$$\phi = \arctan 2 \left(\frac{e - r \sin \zeta}{s - r \cos \zeta} \right) - \zeta \quad (5)$$

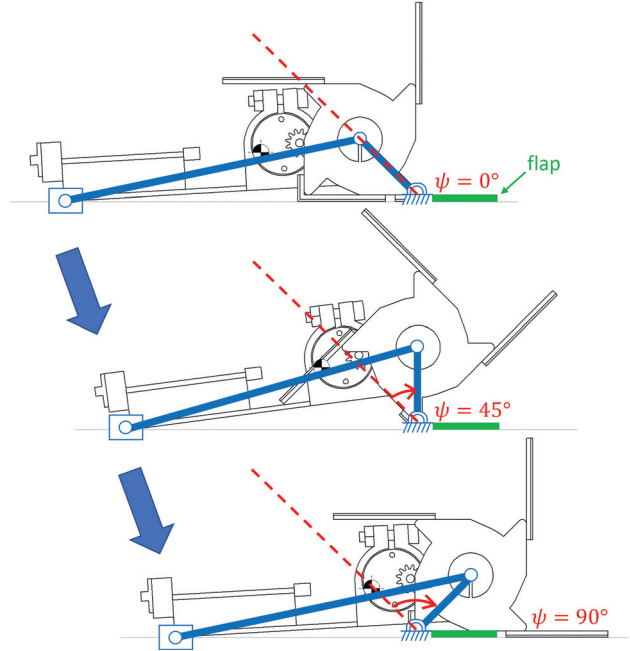


Fig. 3 Slider-crank mechanism model for the robot motion

Note that the robot's motion of $\psi = 0$ deg to $\psi = 90$ deg in Fig. 3 is equivalent to the slider-crank input rotation of $\zeta = 135$ deg to $\zeta = 45$ deg in Fig. 4, i.e., $\zeta = 135$ deg $- \psi$. Using this motion model, the changing geometric parameters of the robot can be captured continuously as it moves, and the force analysis can be performed throughout the robot motion.

3.2 Adhesive Force Requirement Analysis. Adhesives generally have high shear adhesion strength and detachment usually occurs due to insufficient normal adhesion. As seen in Fig. 3, there are generally two states of the robots: double-flap stance and single-flap stance. Similar to Ref. [21], the minimum normal adhesive force required to prevent detachment is analyzed at the single-flap stance as there is only one flap per side attached to the surface providing adhesion. However, instead of assuming that the highest adhesion required is at $\psi = 45$ deg (due to the robot's CG being the furthest away from the surface), we analyze the required normal adhesive force for the entire robot motion and demonstrate that the assumption does not necessarily hold. Although the peeling motion in whigs is gradual, i.e., there exists double-flap stance between $\psi = 0$ deg to $\psi = 90$ deg, the instances are simplified and the analysis of the single-flap stance is performed for the whole motion of the robot, as getting a higher minimum adhesive force than required does not deteriorate the design criteria but rather adds a decent safety margin. The green

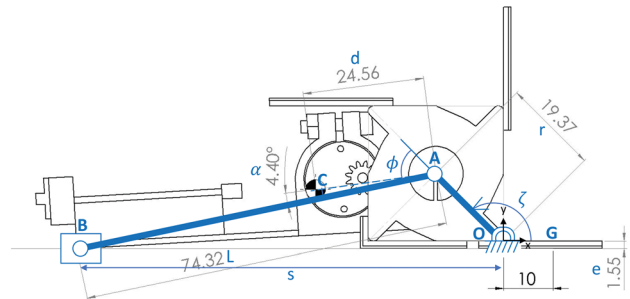


Fig. 4 Geometric parameters of the robot

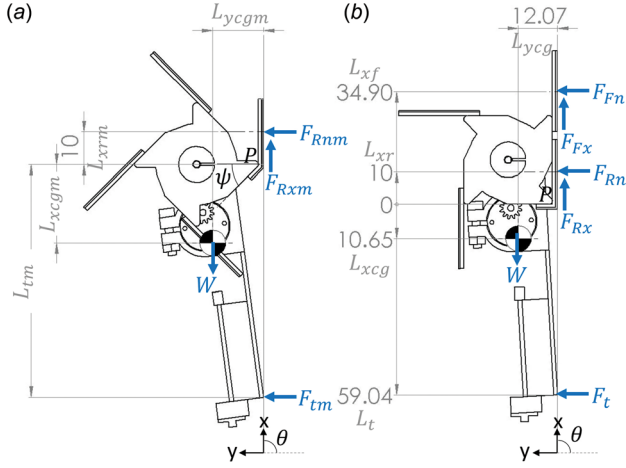


Fig. 5 Free body diagram of the climbing robot (a) during single-stance motion and (b) during double-stance (dimensions are in mm)

adhesive in Fig. 3 is the single flap of interest that provides the adhesion to the surface during the robot motion.

Quasi-static analysis is usually adequate when the robot is moving slowly or at a constant velocity. In addition, assuming symmetric loading and an equivalent point force acting at the center of the adhesive (\mathbf{G} in Fig. 4), the system of equations for equilibrium during single-flap stance (Fig. 5(a)) is given by

$$\sum F_x = 0 = F_{Rxm} - W \sin \theta \quad (6)$$

$$\sum F_y = 0 = F_{tm} + F_{Rnm} - W \cos \theta \quad (7)$$

$$\sum M_P = 0 = F_{tm}L_{tm}(\psi) - W \cos \theta(L_{xcgm}(\psi)) - W \sin \theta(L_{ycgm}(\psi)) - F_{Rnm}L_{xrm} \quad (8)$$

where θ is the climbing slope angle, W is the robot's weight, F_{Rxm} is the shear force on the adhesive flap, F_{Rnm} and F_{tm} are the normal forces on the adhesive and the tail, respectively, L_{tm} , L_{xcgm} , and L_{xrm} are the distances between the pivot point P and the tail, CG, and the center of the adhesive, respectively, L_{ycgm} is distance between the slope surface and the CG, and ψ is the wheel rotation angle. Solving for F_{Rnm} gives

$$F_{Rnm} = \frac{W[\cos \theta(L_{tm}(\psi) - L_{xcgm}(\psi)) - \sin \theta(L_{ycgm}(\psi))]}{L_{tm}(\psi) + L_{xrm}} \quad (9)$$

which yields the normal force acting at the center of the adhesive during the single-stance motion at each instance ψ for different slope angle θ , and where

$$L_{tm}(\psi) = -B_x(\psi) \quad (10)$$

$$L_{xcgm}(\psi) = -C_x(\psi) \quad (11)$$

$$L_{ycgm}(\psi) = C_y(\psi) - B_y(\psi) \quad (12)$$

Figure 6 (top) shows the plot of the normal force acting on the adhesive (F_{Rnm}) for the single-flap stance at varying climbing slopes θ . The blue dotted line denotes the values of F_{Rnm} at $\psi = 45$ deg, which is the wheel rotation angle at which the robot's CG is the furthest away from the slope. The blue solid line plots the minimum value of F_{Rnm} along the robot motion, and the orange dash-dot line shows the wheel rotation angle ψ at which the minimum F_{Rnm} occurs. For example, at 100 deg slope, the minimum F_{Rnm} is -0.22 N and the wheel rotation angle ψ at which

this occurs is 69 deg. Hence, one can see that the minimum force does not always occur at $\psi = 45$ deg; in fact it smoothly progresses from $\psi = 0$ deg to $\psi = 90$ deg for an interval of the slope angles before settling at either $\psi = 0$ deg or $\psi = 90$ deg. This is because, as can be inferred from Eq. (9), the minimum F_{Rnm} is not only affected by the distance of the CG from the surface but also by the relative distance of the robot's tail from other parts of the robot.

Zooming in into details, the robot position where minimum F_{Rnm} occurs for the varying climbing slopes θ (Fig. 6, top) can generally be divided into three regions (Fig. 6, bottom subplots): (i) $F_{Rnm}(\psi)$ increases along the robot motion or is concave and minimum F_{Rnm} occurs at $\psi = 0$ deg, (ii) $F_{Rnm}(\psi)$ is convex and minimum F_{Rnm} progressively occurs at $\psi = 0$ deg to $\psi = 90$ deg, and (iii) $F_{Rnm}(\psi)$ decreases along the robot motion or is concave and minimum F_{Rnm} occurs at $\psi = 90$ deg. This is analogous to scanning a general graph of " $a \cos(x) - b \sin(x)$ " with varying amplitudes, which is foreseen from the structure of Eq. (9).

3.3 Tail Force Analysis. For a more comprehensive analysis of the factors affecting the normal force on the adhesive, we now further analyze the force acting on the robot's tail as well. Figure 7 shows the plot of the minimum normal force on the adhesive for varying slope angles, and the corresponding normal force acting on the robot's tail (F_{tm}) obtained through Eq. (7). Fundamentally, adhesion is required when these forces are negative, as this means that instead of experiencing a positive reaction (pushing) force from the surface, the robot experiences an attractive (pulling) force, which should be provided by the adhesion.

As seen in Fig. 7, F_{tm} falls below zero for a range of slope angles. This means that adhesion at the robot's tail is sometimes needed to maintain equilibrium. However, there is no adhesion at the tail of our robot, and when F_{tm} is negative, the tail in fact loses contact with the surface. In light of this, we now introduce another two distinct states of the robot: (1) the tail is in contact with the surface, and (2) the tail loses contact with the surface. When the second state occurs, we need to set F_{tm} to zero instead. Then, from Eq. (7), F_{Rnm} bears all the y-component of the robot's weight, i.e., $F_{Rnm} = W \cos \theta$. The moment component initially provided by the tail ($F_{tm}L_{tm}$ in Eq. (8)) now needs to be provided by the moment component of the adhesion (termed as M_{Rm} hereafter), which was assumed to be zero or nonexistent in the previous analysis. In summary,

State 1: Robot's tail is in contact with the surface ($F_{tm} > 0$)

$$F_{Rnm} = \frac{W[\cos \theta(L_{tm}(\psi) - L_{xcgm}(\psi)) - \sin \theta(L_{ycgm}(\psi))]}{L_{tm}(\psi) + L_{xrm}} \quad (13)$$

$$F_{tm} = W \cos \theta - F_{Rnm}$$

$$M_{Rm} = 0$$

State 2: Robot's tail loses contact with the surface ($F_{tm} \leq 0$)

$$F_{Rnm} = W \cos \theta$$

$$F_{tm} = 0$$

$$M_{Rm} = -W \cos \theta(L_{xcgm}(\psi)) - W \sin \theta(L_{ycgm}(\psi)) - F_{Rnm}L_{xrm} \quad (14)$$

Figure 8 shows the plots of the minimum normal forces on the adhesive obtained using the different analysis approaches, with F_{Rnm} (rev) and F_{tm} (rev) being the results of the revised analysis in this section. As seen from the figure, fixing the force analysis at $\psi = 45$ deg and without analyzing the force behavior at the robot's tail leads to an underestimation of the minimum adhesive force required. It is also more sensible to set $F_{tm} = 0$ when $F_{tm} \leq 0$, as following the previous analysis (F_{Rnm} (min)), one would have expected the robot (without adhesive at the tail) to be able to climb a 260 deg slope without the need of an adhesive on

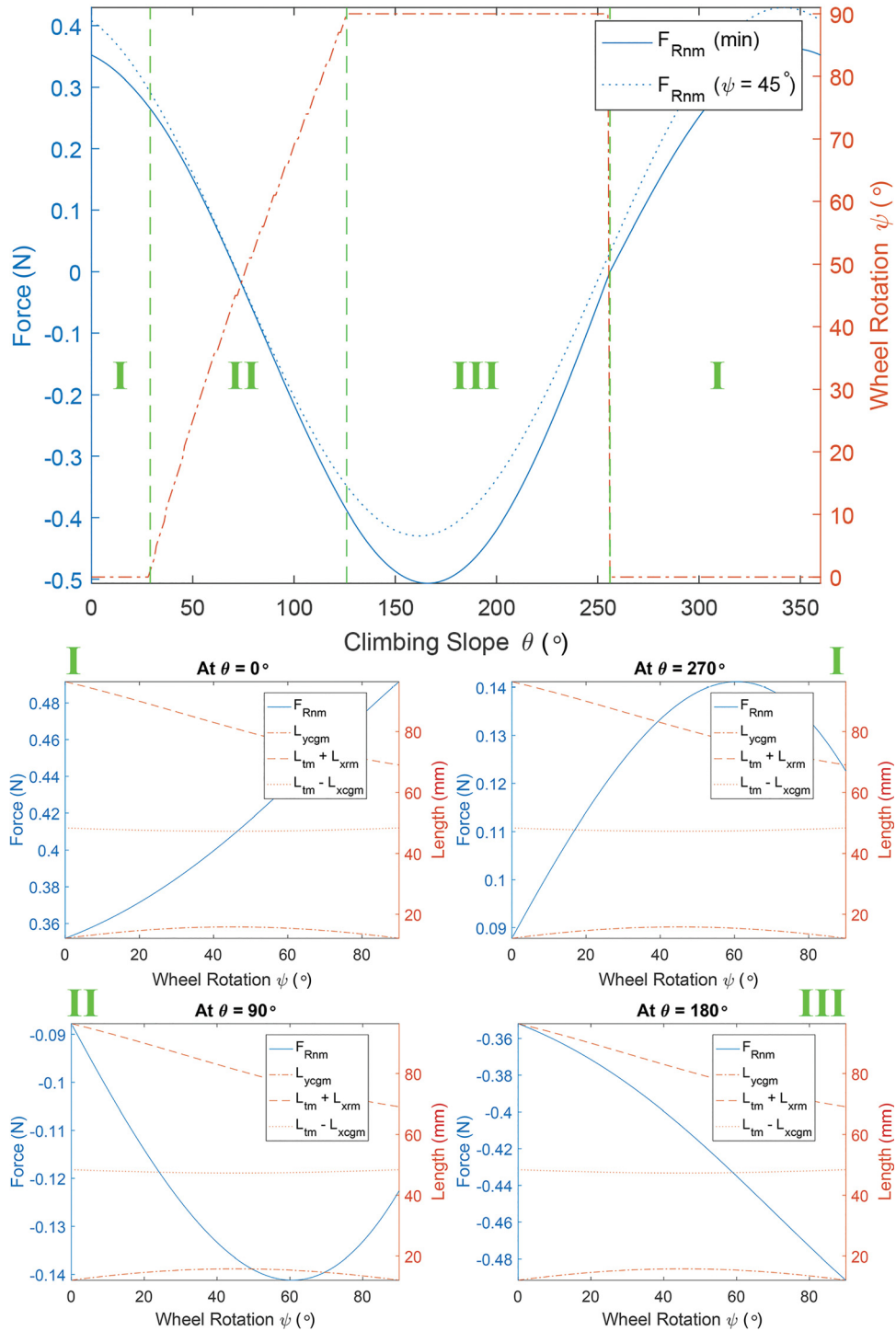


Fig. 6 Plot of the normal force at the center of the adhesive during single-flap stance versus slope angle (top), and along the robot motion at several specific slope angles (bottom subplots)

the wheels, which is not the case. The revised analysis (F_{Rnm} (rev) in Fig. 8) gives a more reasonable prediction as the robot is expected to stop needing an adhesive for slopes above 270° deg (climbing vertical down).

Based on the minimum normal force acting on the adhesive (F_{Rnm} (rev) in Fig. 8), we can then decide on the required value of the *critical peeling force*, F_{cr} , of the adhesive material according to the slope angle that the robot needs to be able to climb, with $F_{cr} = -F_{Rnm}$. For example, in our case, we want to design a robot that is able to climb up to 120° deg slope, so the critical peeling

force of the adhesive material used should be at least 0.36 N, as shown in Fig. 8 (red dashed line).

3.4 Preload-to-Peeling Force Ratio Analysis. Another important measure in the modeling of climbing robots with dry adhesives is the preload-force-to-critical-peeling-force ratio, as an adhesive material is usually characterized by how much adhesive force can be generated by a given preload force. Analyzing the double-flap stance (Fig. 5(b)), it can be inferred that at this stage

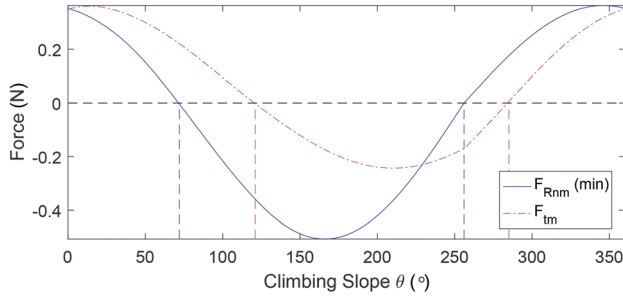


Fig. 7 Plot of the minimum normal force at the center of the adhesive during single-flap stance, and the corresponding normal force acting on the robot's tail for varying slope angles

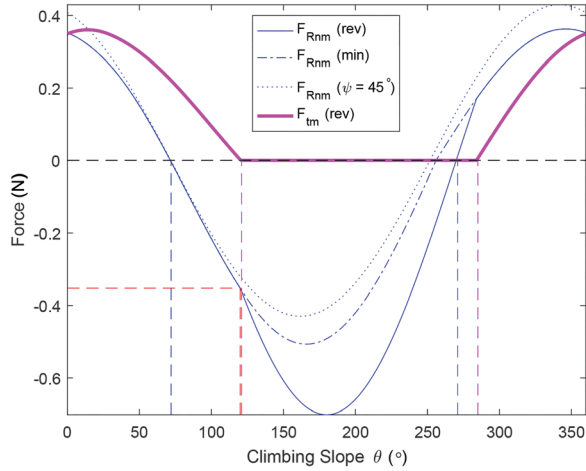


Fig. 8 Plot of the minimum normal force at the center of the adhesive during a single-flap stance based on the different analysis approaches, and the force acting on the robot's tail based on the tail force analysis, for varying slope angles

the rear flap is peeling the adhesive while the front flap is being preloaded simultaneously. Assuming that peel-off is just about to occur, then $F_{Rn} = -F_{cr}$, and F_{Fn} gives the preload force applied on the front flap. The system of equations for equilibrium during double-flap stance (Fig. 5(b)) is given by

$$\sum F_x = 0 = F_{Rx} + F_{Fx} - W \sin \theta \quad (15)$$

$$\sum F_y = 0 = F_t + F_{Rn} + F_{Fn} - W \cos \theta \quad (16)$$

$$\sum M_P = 0 = F_t L_t - W \cos \theta (L_{xcg}) - W \sin \theta (L_{ycg}) - F_{Rn} L_{xr} - F_{Fn} L_{xf} \quad (17)$$

from which we can solve for F_{Fn} with the geometric dimensions of the robot as given in Fig. 5(b). Similarly, there are two states of the robot.

State 1: Robot's tail is in contact with the surface ($F_t > 0$)

$$F_{Fn} = \frac{W [\cos \theta (L_t - L_{xcg}) - \sin \theta (L_{ycg})] - F_{Rn} (L_t + L_{xr})}{L_t + L_{xf}}$$

$$F_t = W \cos \theta - F_{Rn} - F_{Fn}$$

$$M_R + M_F = 0 \quad (18)$$

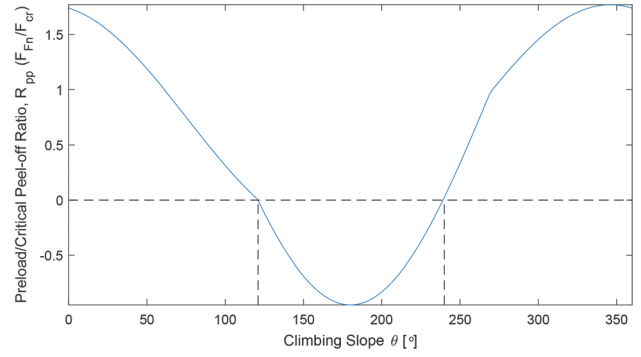


Fig. 9 Plot of the preload-to-critical-peeling force ratio for varying slope angles

State 2: Robot's tail loses contact with the surface ($F_t \leq 0$)

$$F_{Fn} = W \cos \theta - F_{Rn}$$

$$F_t = 0$$

$$M_R + M_F = -W \cos \theta (L_{xcg}) - W \sin \theta (L_{ycg}) - F_{Rn} L_{xr} - F_{Fn} L_{xf} \quad (19)$$

where M_R and M_F are the moment components of the rear and front adhesive, respectively. The preload-to-critical-peel-off ratio (R_{pp}) can then be obtained as F_{Fn}/F_{cr} and is plotted in Fig. 9. Negative values of the ratio indicate the range of climbing slopes that the robot is unable to climb due to the choice of the critical peeling force F_{cr} value of the adhesive material. This ratio will be useful in devising further requirements for the adhesive material, which will be discussed in Sec. 4.

4 Climbing Robot Requirements

In this section, we discuss two important design criteria that can be obtained following the force analysis, namely the minimum adhesive size to generate the required adhesion force based on the material characteristics, and the minimum motor torque required to provide the peeling and preload forces, overcome the robot's weight component along the slope, and keep the overall equilibrium of the climbing robot. These two criteria must be met in order to attain an operative climbing robot, which can also serve as constraints for robot optimization.

4.1 Adhesive Size Requirement. The performance characteristic curve of an adhesive material in terms of how much adhesive force is generated given a preload force can be approximated by a power law function [21]

$$P_A = a P_P^{1/n} \quad (20)$$

where P_A is the adhesion pressure, P_P is the preload pressure, a is a scaling coefficient, and $n > 1$. The characteristics of the bilayer adhesive used here based on the adhesive characterization experiment conducted can be approximated by $P_A = 0.675 P_P^{2/3}$. In order to identify the suitable size of the adhesive material, the adhesion versus preload curve is overlaid with lines of gradient values corresponding to the inverse of the preload-to-peeling ratio R_{pp} at various climbing slope angle θ (Fig. 9)

$$P_A = \frac{1}{R_{pp}(\theta)} P_P \quad (21)$$

This is shown in Fig. 10 for some slope angles. The intersection of the performance curve and this inverse-ratio line then gives the specific preload pressure that multiplies into the required amount

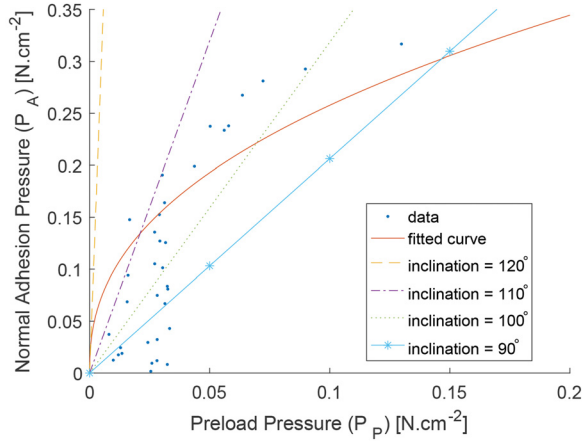


Fig. 10 Adhesive performance curve overlaid with lines of gradient values of the inverse of the preload-to-peeling ratio for several slope angles

of adhesion pressure according to the preload-to-peeling ratio, which can be obtained as

$$P_p^* = (aR_{pp})^{\frac{1}{n-1}} \quad (22)$$

The minimum required adhesive area (A_a) is obtained by

$$A_a = \frac{F_{Fn}}{P_p^*} \quad (23)$$

Based on this analysis and the bilayer adhesive material characterization, our robot is required to have a minimum adhesive area of 6.8 cm^2 per flap to be able to climb up to 120° slope angle.

4.2 Motor Torque Requirement. To obtain the minimum motor torque required, the free body diagram (FBD) of the whole robot is decoupled into the wheel and chassis components as shown in Fig. 11. The values of the normal forces acting on the

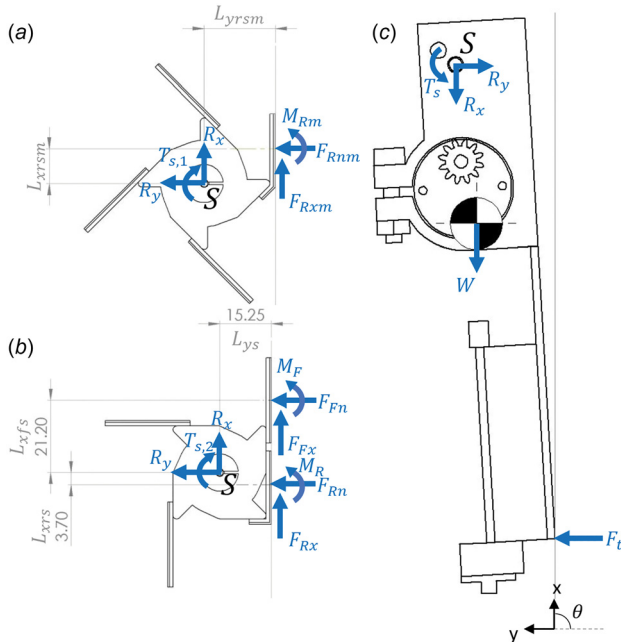


Fig. 11 Free body diagram of the individual components of the robot: (a) wheel at single-flap stance, (b) wheel at double-flap stance, and (c) chassis

adhesive and the tail will follow the revised analysis based on the robot motion and tail consideration ($F_{Rnm}(\text{rev})$). From the chassis FBD (Fig. 11(c)), we have

$$\sum F_x = 0 = -R_x - W \sin \theta \quad (24)$$

From the single-flap stance wheel FBD (Fig. 11(a)), we have

$$\sum F_x = 0 = F_{Rxm} + R_x \quad (25)$$

$$\sum M_S = 0 = T_{s,1} - F_{Rnm}(L_{xrs}(\psi)) - F_{Rxm}(L_{yrs}(\psi)) - M_{Rm} \quad (26)$$

where

$$L_{xrs}(\psi) = G_x - A_x(\psi) \quad (27)$$

$$L_{yrs}(\psi) = A_y(\psi) - B_y(\psi) \quad (28)$$

Then, we can get the torque acting on the shaft at single-flap stance along the robot motion as

$$T_{s,1} = F_{Rnm}(L_{xrs}(\psi)) + W \sin \theta (L_{yrs}(\psi)) + M_{Rm} \quad (29)$$

Similarly, from the double-flap stance wheel FBD (Fig. 11(b)) we have

$$\sum F_x = 0 = F_{Rx} + F_{Fx} + R_x \quad (30)$$

$$\sum M_S = 0 = T_{s,2} + F_{Rn}(L_{xrs}) - F_{Fn}(L_{xfs}) - (F_{Rx} + F_{Fx})L_{ys} - M_R - M_F \quad (31)$$

The torque acting on the shaft during double-flap stance is then obtained as

$$T_{s,2} = F_{Fn}(L_{xfs}) - F_{Rn}(L_{xrs}) - W \sin \theta (L_{ys}) + M_R + M_F \quad (32)$$

Then, the minimum motor torque requirement is obtained as

$$T_m = \frac{\max(\max(T_{s,1}), T_{s,2})}{R_g} \quad (33)$$

where R_g is gear reduction value (if any).

Figure 12 shows the minimum motor torque required by our robot to climb the varying slope angles with adhesive material of critical peeling force $F_{cr} = 0.36 \text{ N}$. Note that since our robot is driven by two separate motors, the required torque is shared by the two motors.

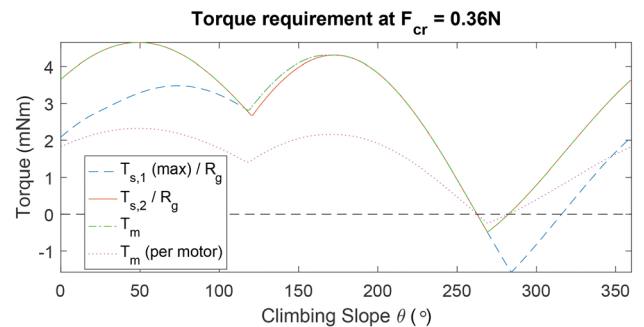


Fig. 12 Plots of the torque requirements for varying slope angles for $F_{cr} = 0.36 \text{ N}$

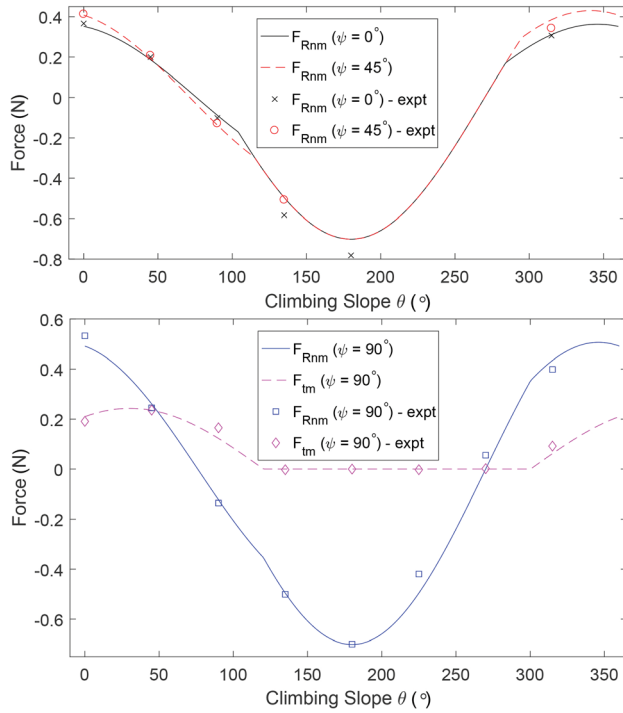


Fig. 13 Comparison between theoretical and experimental values of the normal force on the adhesive at the beginning ($\psi = 0$ deg) and middle ($\psi = 45$ deg) of single-flap stance (top), and both the normal force on the adhesive and tail at the end ($\psi = 90$ deg) of single-flap stance (bottom)

5 Experiments

In this section, we perform experiments on the physical climbing robot prototype to verify the validity of the revised force analysis and the design criteria generated.

5.1 Force Evaluation. To verify the normal force acting on the adhesive along the robot's motion, one of the robot's legs was adhered to a digital balance with a range of ± 300 g and a precision of 0.01 g to measure the normal force at three different single-flap stance configurations as shown in Fig. 3. These measurements were taken at a climbing slope interval of 45 deg, and the results are shown in Fig. 13 (top). It was challenging to acquire reliable measurements at robot's configuration $\psi = 0$ deg and $\psi = 45$ deg for climbing slope angles 180 deg, 225 deg, and 270 deg, as the robot tended to slowly rotate away from the surface under its own weight (pitch-back) due to the compliancy of the adhesive. At $\psi = 90$ deg, this pitch-back moment was counteracted by the higher bending moment of the adhesive at the larger bending angle, and thus measurement could be taken. In light of this, the force measurement at the tail was only performed at configuration $\psi = 90$ deg so that it was not affected by the pitch-back motion. For the tail force measurement, the robot's tail was placed on a digital scale (without adhesive), and the force measurement results are shown in Fig. 13 (bottom). Based on the experimental results, it is verified that the force behavior during the robot's motion can be attained fairly accurately using the robot motion model. The experimental results also validate that the normal force at the tail became zero when it loses contact with the sensor (i.e., the surface) instead of experiencing a negative force, and the corresponding force on the adhesive to overcome this is also verified.

5.2 Design Criteria Verification and Discussions. We now compare the design criteria obtained for our robot against the performance of the physical robot prototype. Upon testing the physical robot, it was found that the robot was able to climb a



Fig. 14 Image sequence of the robot climbing a vertical surface

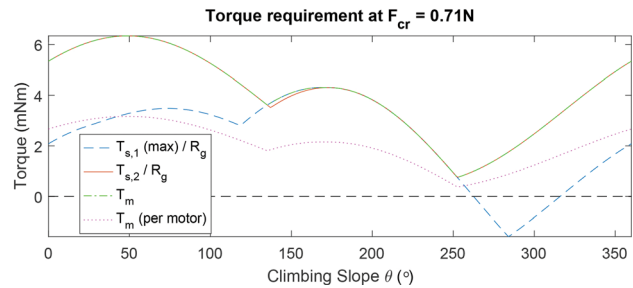


Fig. 15 Torque requirements for critical peeling force designed to climb all slope angles

120 deg slope with a minimum adhesive area of 7 cm^2 per flap, which is very close to the adhesive size requirement obtained from the analysis. The design criteria generated here are more accurate than in our previous work [32] as in this work we did our own characterization of the bilayer adhesive material. Figure 14 shows an image sequence of our robot climbing a vertical surface during one of the tests. The robot climbs the vertical surface at an average speed of 3 cm/s.

Although the design criteria slightly underestimated the actual required adhesive area, it provides a reasonable guideline and starting estimate on the adhesive requirement. Possible reasons for the larger actual size required include incomplete contact area between the adhesive and the surface, nonideal force transfer during the step, and overestimation of the adhesion performance curve as material test is usually conducted in a highly controlled environment. It is also recommended [21] to have a margin of safety by increasing the area of the adhesive to circumvent those expected failures.

Based on Fig. 12, the torque required by each motor of our robot to climb slopes up to 120 deg is on average around 2 mN-m. To verify the torque specification, we test the robot using two different motors: a low torque motor at 2.1 mN-m (Faulhaber 1512U003SR, (Schönaich, Germany) 13:1 running at 75% continuous torque capacity) and a high torque motor at 14.85 mN-m (Faulhaber 1512U003SR 112:1 running at 75% continuous torque capacity). The robot with the low torque motor was barely able to walk intermittently even on a 0 deg slope, while the robot with high torque motor climbed the slope up to 120 deg smoothly. These tests verify the motor torque criteria provided by the analysis.

The torque requirement analysis also provides explanation for the observation or experimental results in Ref. [17]. Their robot, which has a similar structure as our climbing robot, is capable of climbing on all slope angles. Hence, it will have a similar form of motor torque requirement plot as shown in Fig. 15, which is the plot of the required motor torque should our robot have been designed to climb on all slope angles ($F_{cr} = 0.71$ N from Fig. 8).

Their robot was reported to climb slower vertically up than inverted on the ceiling, which is verified by the higher motor torque required at 90 deg slope than at 180 deg. They also reported that the robot failed to walk vertically down due to the body rotating too much under its own weight during the single-flap stance. This is again verified by the motor torque requirement which shows a negative torque requirement for the single-flap stance at 270 deg, which is mainly attributed by the robot's weight component.

6 Conclusions

In this work, we expand on a previously reported approach for climbing robot analysis and also apply it to the design of our climbing robot. Several refinements of the approach that were previously absent include integrating a robot motion model in order to obtain a more extensive and accurate force behavior analysis along the robot's motion, investigating the tail's effect on the climbing robot's overall equilibrium and requirements, and verification of the design criteria. Based on the more comprehensive analysis, we introduce and discuss two additional distinct states of the robot: when the robot's tail is in contact with the surface and when the robot's tail loses contact with the surface, which affects the overall force analysis of the climbing robot. The force behavior along the robot's motion and the two states of the robot's tail proposed in this paper are verified through experimental force measurements. Future works will include sensitivity analysis on the developed model to optimally test and design the wheel configuration, as well as optimization of the drive train components and mass distribution.

Acknowledgment

The authors gratefully acknowledge the support of TL@SUTD-Systems Technology for Autonomous Reconnaissance and Surveillance and SUTD-MIT International Design Center.²

Funding Data

- Ministry of Defence (IGDST130101, Funder ID. 10.13039/100009941).

References

- [1] Chamanbaz, M., Mateo, D., Zoss, B. M., Tokić, G., Wilhelm, E., Bouffanais, R., and Yue, D. K., 2017, "Swarm-Enabling Technology for Multi-Robot Systems," *Front. Rob. AI*, 4, p. 12.
- [2] Grocholsky, B., Keller, J., Kumar, V., and Pappas, G., 2006, "Cooperative Air and Ground Surveillance," *IEEE Rob. Autom. Mag.*, 13(3), pp. 16–25.
- [3] Chowdhury, A. R., Soh, G. S., Foong, S. H., and Wood, K. L., 2018, "Implementation of Caterpillar Inspired Roll and Nonlinear Control Strategy in a Spherical Robot," *J. Bionic Eng.*, 15(2), pp. 313–328.
- [4] Hariri, H. H., Soh, G. S., Foong, S. H., and Wood, K. L., 2018, "Locomotion Study of a Standing Wave Driven Piezoelectric Miniature Robot for Bi-Directional Motion," *IEEE Trans. Rob.*, 33(3), pp. 742–747.
- [5] Rybski, P. E., Papanikolopoulos, N. P., Stoeter, S. A., Krantz, D. G., Yesin, K. B., Gini, M., Voyles, R., Hougen, D. F., Nelson, B., and Erickson, M. D., 2000, "Enlisting Rangers and Scouts for Reconnaissance and Surveillance," *IEEE Rob. Autom. Mag.*, 7(4), pp. 14–24.
- [6] Dan, Z., Tianmiao, W., Jianhong, L., and Guang, H., 2004, "Modularization of Miniature Tracked Reconnaissance Robot," IEEE International Conference on Robotics and Biomimetics (ROBIO), Shenyang, China, Aug. 22–26, pp. 490–494.
- [7] Xiao, J., Morris, W., Chakravarthy, N., and Calle, A., 2006, "City Climber: A New Generation of Mobile Robot With Wall-Climbing Capability," Unmanned Systems Technology VIII, IntechOpen Limited, London, p. 62301D.
- [8] Tâche, F., Fischer, W., Siegwart, R., Moser, R., and Mondada, F., 2007, "Compact Magnetic Wheeled Robot With High Mobility for Inspecting Complex Shaped Pipe Structures," IEEE/RSJ International Conference on Intelligent Robots and Systems (IROS), San Diego, CA, Oct. 29–Nov. 2, pp. 261–266.
- [9] Sintov, A., Avramovich, T., and Shapiro, A., 2011, "Design and Motion Planning of an Autonomous Climbing Robot With Claws," *Rob. Auton. Syst.*, 59(11), pp. 1008–1019.

- [10] Prahlad, H., Pelrine, R., Stanford, S., Marlow, J., and Kornbluh, R., 2008, "Electroadhesive Robots Wall Climbing Robots Enabled by a Novel, Robust, and Electrically Controllable Adhesion Technology," IEEE International Conference on Robotics and Automation (ICRA), Pasadena, CA, May 19–23, pp. 3028–3033.
- [11] Daltorio, K. A., Gorb, S., Peressadko, A., Horschler, A. D., Ritzmann, R. E., and Quinn, R. D., 2006, "A Robot That Climbs Walls Using Micro-Structured Polymer Feet," International Conference on Climbing and Walking Robots (CLAWAR), Brussels, Belgium, Sept. 12–14, pp. 131–138.
- [12] Kim, S., Spenko, M., Trujillo, S., Heyneman, B., Santos, D., and Cutkosky, M. R., 2008, "Smooth Vertical Surface Climbing With Directional Adhesion," *IEEE Trans. Rob.*, 24(1), pp. 65–74.
- [13] Unver, O., and Sitti, M., 2009, "A Miniature Ceiling Walking Robot With Flat Tacky Elastomeric Footpads," IEEE International Conference on Robotics and Automation (ICRA), Kobe, Japan, May 12–17, pp. 2276–2281.
- [14] Powelson, M. W., and Canfield, S. L., 2017, "Design of Track-Based Climbing Robots Using Dry Adhesives," *ASME Paper No. V05BT08A020*.
- [15] Raut, H. K., Baji, A., Hariri, H. H., Parveen, H., Soh, G. S., Low, H. Y., and Wood, K. L., 2018, "Gecko-Inspired Dry Adhesive Based on Micro-Nanoscale Hierarchical Arrays for Application in Climbing Devices," *ACS Appl. Mater. Interfaces*, 10(1), pp. 1288–1296.
- [16] Sahay, R., Low, H. Y., Baji, A., Foong, S., and Wood, K. L., 2015, "A State-of-the-Art Review and Analysis on the Design of Dry Adhesion Materials for Applications Such as Climbing Micro-Robots," *RSC Adv.*, 5(63), pp. 50821–50832.
- [17] Breckwoldt, W. A., Daltorio, K. A., Heepe, L., Horschler, A. D., Gorb, S. N., and Quinn, R. D., 2015, "Walking Inverted on Ceilings With Wheel-Legs and Micro-Structured Adhesives," IEEE/RSJ International Conference on Intelligent Robots and Systems (IROS), Hamburg, Germany, Sept. 28–Oct. 2, pp. 3308–3313.
- [18] Murphy, M. P., Tso, W., Tanzini, M., and Sitti, M., 2006, "Waalbot: An Agile Small-Scale Wall Climbing Robot Utilizing Pressure Sensitive Adhesives," IEEE/RSJ International Conference on Intelligent Robots and Systems (IROS), Beijing, China, Oct. 9–15, pp. 3411–3416.
- [19] Daltorio, K. A., Horschler, A. D., Gorb, S., Ritzmann, R. E., and Quinn, R. D., 2005, "A Small Wall-Walking Robot With Compliant, Adhesive Feet," IEEE/RSJ International Conference on Intelligent Robots and Systems (IROS), Edmonton, AB, Canada, Aug. 2–6, pp. 3648–3653.
- [20] Daltorio, K. A., Wei, T. E., Gorb, S. N., Ritzmann, R. E., and Quinn, R. D., 2007, "Passive Foot Design and Contact Area Analysis for Climbing Mini-Whegs," IEEE International Conference on Robotics and Automation (ICRA), Roma, Italy, Apr. 10–14, pp. 1274–1279.
- [21] Murphy, M. P., and Sitti, M., 2007, "Waalbot: An Agile Small-Scale Wall-Climbing Robot Utilizing Dry Elastomer Adhesives," *IEEE/ASME Trans. Mechatronics*, 12(3), pp. 330–338.
- [22] Carelli, C., Déplace, F., Boissonnet, L., and Creton, C., 2007, "Effect of a Gradient in Viscoelastic Properties on the Debonding Mechanisms of Soft Adhesives," *J. Adhes.*, 83(5), pp. 491–505.
- [23] King, D. R., Bartlett, M. D., Gilman, C. A., Irschick, D. J., and Crosby, A. J., 2014, "Creating GeckoLike Adhesives for "Real World" Surfaces," *Adv. Mater.*, 26(25), pp. 4345–4351.
- [24] Bartlett, M. D., Croll, A. B., King, D. R., Paret, B. M., Irschick, D. J., and Crosby, A. J., 2012, "Looking Beyond Fibrillar Features to Scale Geckolike Adhesion," *Adv. Mater.*, 24(8), pp. 1078–1083.
- [25] Bartlett, M. D., Croll, A. B., and Crosby, A. J., 2012, "Designing BioInspired Adhesives for Shear Loading: From Simple Structures to Complex Patterns," *Adv. Funct. Mater.*, 22(23), pp. 4985–4992.
- [26] Bartlett, M. D., and Crosby, A. J., 2014, "High Capacity, Easy Release Adhesives From Renewable Materials," *Adv. Mater.*, 26(21), pp. 3405–3409.
- [27] 3M, 2018, "3M VHB Tape Design Guide," St. Paul, MN, accessed Jan. 11, 2019, <http://multimedia.3m.com/mws/media/12041680/3m-vhb-tape-design-guide-high-res-pdf.pdf>
- [28] Liew, K. C. W., 2017, "Fabrication and Characterization of Biomimetic Dry Adhesives Supported by Foam Backing Material," Master's thesis, University of Waterloo, Waterloo, ON, Canada.
- [29] Shahsavan, H., and Zhao, B., 2013, "Bioinspired Functionally Graded Adhesive Materials: Synergetic Interplay of Top Viscous Elastic Layers With Base Micropillars," *Macromolecules*, 47(1), pp. 353–364.
- [30] Hariri, H. H., Koh, D. C. Y., Lim, H. C., Dharmawan, A. G., Nguyen, V. D., Soh, G. S., Foong, S., Bouffanais, R., Low, H. Y., and Wood, K. L., 2018, "ORION-II: A Miniature Climbing Robot With Bilayer Compliant Tape for Autonomous Intelligent Surveillance and Reconnaissance," IEEE 15th International Conference on Control, Automation, Robotics and Vision (ICARCV), Singapore, Nov. 18–21.
- [31] McCarthy, J. M., and Soh, G. S., 2010, "Geometric Design of Linkages," *Interdisciplinary Applied Mathematics*, 2nd ed., Springer Science and Business Media, New York.
- [32] Dharmawan, A. G., Xavier, P., Anderson, D., Perez, K. B., Hariri, H. H., Soh, G. S., Baji, A., Bouffanais, R., Foong, S., Lee, H. Y., and Wood, K. L., 2018, "A Bio-Inspired Miniature Climbing Robot With Bilayer Dry Adhesives: Design, Modeling, and Experimentation," *ASME Paper No. V05BT07A036*.

²<http://fdc.sutd.edu.sg>